Int. J. Electrochem. Sci., 15 **(2020)** 1169 – 1186, doi: 10.20964/2020.02.22

International Journal of ELECTROCHEMICAL SCIENCE
www.electrochemsci.org

Modification Structure of CoS_2 Electrocatalysts towards Enhanced Oxygen Evolution by Nitrogen Doping

Wenshu Yang[1,2], *Zhigang Chen*[2,1,*], *Huaming Li*[3,*]

[1] Jiangsu University Jingjiang College, Jiangsu University, Zhenjiang, China
[2] School of the Environment and Safety Engineering, Jiangsu University, Zhenjiang, China
[3] Institute for Energy Research, Jiangsu University, Zhenjiang, China
[*]E-mail: chenzhigang001@163.com, lihm@ujs.edu.cn

Received: 7 October 2019 / *Accepted:* 19 November 2019 / *Published:* 31 December 2019

The sluggish kinetics of the electrochemical oxygen evolution reaction (OER) usually requires using precious metal-based electrocatalysts to lower energy barriers. Designing and developing highly efficient and stable electrocatalysts made of nonprecious elements for OER remain a significant challenge. Herein, a fabrication of nitrogen-doped CoS_2 via a facile method, and their different electrocatalytic performance in response to variations in nitrogen doping is demonstrated. Urea and NH_4F are nitrogen containing reactants whose amino groups have a strong interaction with Co^{2+} ions, resulting in a nitrogen containing precursor. After a sulfidation process, nitrogen doped CoS_2 is obtained. An addition of a hydrogen annealing step enables the nitrogen doping process to load between 0 and 13.6%. Nitrogen doping has a significant effect on the distribution of sulfur in CoS_2, which significantly improves the quality or quantity of active sites. As a result, the nitrogen-doped CoS_2 shows high electrochemical activity toward OER. Notably, the N_4-CoS_2-400 sample exhibits a small overpotential of 290 mV to provide a current density of 10 mA cm^{-2}. The results in this study provide information for the utilization of heteroatoms in a rational design for enhancing electrochemical performance toward OER and may create new opportunities in other energy-related areas.

Keywords: Nitrogen doped CoS_2, Hydrogen annealing, OER, heteroatom, elctrocatalysts.

1. INTRODUCTION

The rapid development of modern society and the increased population has already resulted in increasing energy demands and impending climate change. As a result, growing concern has been focused on clean technologies as feasible alternatives to diminishing fossil fuels, such as low-temperature fuel cells, electrolysis, and photoelectrochemical water splitting [1]. Electrochemical technologies can convert energy into widely used and practical chemical and fuel with little or no pollution. Among the most appealing options, electrochemical water splitting is taking center stage for the hydrogen economy because it stands out as a viable option for eventual applications [2]. Electrochemical water splitting involves a hydrogen evolution reaction (HER) on the cathode and an oxygen evolution reaction (OER) on the anode. Of the two half reaction, OER is a multistep electron transfer process, which suffers from sluggish kinetics and is considered a bottleneck for the overall water splitting reaction. Currently, precious metal-based materials (e.g, Pt, IrO_2, RuO_2) still play a dominant role as the most efficient and durable water splitting electrocatalysts. However, the scarcity of precious metals limits their widespread application. In light of this, tremendous efforts have been undertaken toward the development of cost-effective electrocatalysts. Specifically, transition metal chalcogenides have been widely investigated as particularly promising nonprecious metal-based water splitting electrocatalysts [3]. For example, the first electrochemical performance study of MoS_2 can be traced to the 1970s [4]. The bulk MoS_2 showed dull activity toward water splitting due to its limited number of active sites and low conductivity, hampering its development for a long time. In 2005, Hinnemann et al. found that the (1010) Mo-edge site in layered MoS_2 structure had a close resemblance to the active site of nitrogenase [5], the above discovery significantly boosted the rapid development of MoS_2-related materials [6-8]. In addition, nickel and cobalt are known to be some of the most abundant elements on earth. Zou et al. reported high performance bifunctional electrocatalysts toward HER and OER using high-index faceted Ni_3S_2 nanosheet arrays [9]. Matthew et al. reported that CoS_2 with nanowire morphology had superior HER performance [10]. Kong et al. identified a group of electrocatalysts from first-row transition metal dichalcogenides toward HER [11]. From the results, the FeCoS showed the highest electrochemical performance. Despite the large effort made, the current transition metal dichalcogenides still suffer from high reaction barriers and sluggish kinetics, especially for OER, resulting in a large overpotential. Therefore, a new perspective is key for the rational design and development of transition metal dichalcogenide-based OER electrocatalysts with high efficiency, stability and low cost for water splitting.

In an operating OER cell, the reactants first adsorb on the electrocatalyst surface, and then electrochemical reactions occur through a multistep electron transfer process. Finally the obtained oxygen bubbles desorb from the electrocatalyst surface. The OER operation mainly occurs on an important interface of the electrocatalysts and the electrolyte, and the electrocatalytic properties are in principle determined completely by their surface structure. These mean that the properties of the solid-liquid interphase and the kinetics of electron transfer in this interphase play a critical role in determining the OER performance. Generally, the engineering of an electrocatalyst composition and the construction of a well-defined architecture are two common strategies. Different compositions mainly influence the behaviors of electron transfer and thus promote the kinetics of intermediate adsorption. The methods for composition engineering usually include alloying, vacancy generation, and doping. For example, Sun et al. demonstrated that alloy composition can result in fast electron transport along a nanowire and form a well-defined electronic conformation for proton discharging [12]. Jaramillo et al. reported that the electronic conformation of a mixed metal alloy could pose excellent electronic conformation and thus push the catalysts close to the top of a volcano plot [13]. Shao-Horn et al. demonstrated that the oxygen vacancy could facilitate water uptake and be able to promote electronic conduction in an oxide lattice [14]. Xie et al. further confirmed the uptake effect of oxygen vacancies using DFT calculations [15]. Doping is also an important and useful approach for modifying the electronic conformation [16, 17]. A combined theoretical and experimental study by Song et al. demonstrated that doping could promote intermediate adsorption by tuning the electronic conformation [18]. Sargent et al. showed that a W dopant could provide a well-defined electron conformation for local coordination of the intermediate [19]. The obtained FeCoW oxy-hydroxide shows high OER performance. Hao et al. found that nitrogen doping had a significant effect on the position of the adjacent metal *d* state center, the electron density, and the Gibbs free energy of different intermediate adsorption [20, 21]. Other dopants, such as iron [22], aluminum [23], and nitrogen [24], have also been reported to have a significant effect on the electron conformation. Compared with that of alloying and oxygen vacancies, the doping method is more versatile for regulating the electronic conformation, which can be realized by changing the type or quantity of dopant. Therefore, despite different available approaches, doping methods offer enormous possibilities in promoting OER performance.

Herein, a facile and general two-step approach for an electronic conformation of CoS_2 by employing a nitrogen dopant was demonstrated. Nitrogen-doped CoS_2 is synthesized through a hydrothermal reaction with a post-annealing process. For the hydrothermal reactions, urea and NH_4F not only provide alkaline conditions but also act as nitrogen sources for the precursor to absorb. During the annealing process, the nitrogen atom occupies a site in the crystal lattice, and finally, nitrogen-doped CoS_2 was obtained. Nitrogen atoms bear a relatively higher electronegativity than that of cobalt atoms, suggesting an increased electron occupation in nitrogen atoms and leading to a rearrangement of electrons. Nitrogen doping has a significant effect on the distribution of sulfur, which further influences the electrochemical activity toward OER. By controlling the reaction conditions, the nitrogen doping level can be varied from 0 to 13.6%. We systematically examined the influence of nitrogen doping on the OER performance. The results indicate that all of the nitrogen-doped samples have a more negative current response than that of pure CoS_2. The OER activities decrease when the nitrogen doping decreases. These results imply promising directions for the design of prospective commercial OER elctrocatalysts.

2. EXPERIMENTAL SECTION

2.1. Materials

$CoCl_2 \cdot 6H_2O$, urea, sulfur powder and NH_4F sulfurwere purchased from Sinopharm Chemical Reagent Co. Ltd.. The carbon paper (CP) was bought from Shanghai Hesen Co. Ltd.. Other reagents were AR grade and used as received.

2.2. Preparation of $Co(CO_3)_{0.5}(OH)$ $0.11H_2O$ precursor on CP

The $Co(CO_3)_{0.5}(OH)$ $0.11H_2O$ precursor was first prepared through a modified method reported by previous literature [25]. In a typical experiment, precursors were synthesized by adding

$CoCl_2·6H_2O$ (1 mmol), NH_4F (3 mmol) and urea (5 mmol) to 20 mL distilled water and stirring for 30 min to form a homogeneous solution. A piece of CP with size of 1 cm × 4 cm was immersed into above mixed solution. The mixture was transferred to a 50 mL Teflon-lined autoclave and reacted for 6 h at 120 ºC. After cool to room temperature, the sample was thoroughly rinsed with deionized water and ethanol for several times, then dried at room temperature before used for synthesis of nitrogen doped CoS_2.

2.3. Preparation of nitrogen doped CoS_2 on CP

For synthesis of nitrogen doped CoS_2, the $Co(CO_3)_{0.5}(OH)$ $0.11H_2O$ was annealed with sulfur powder. The $Co(CO_3)_{0.5}(OH)$ $0.11H_2O$ and 500 mg sulfur powder (at the upstream side) were placed separately in a quartz tube and the quartz tube was heated to 300 ºC under a heating rate of 10 °C/min and held for 40 min in nitrogen condition. The obtained sample was named as N_4-CoS_2-300. When the sulfidation temperatures were 400 and 500 ºC, the final samples were donated as N_4-CoS_2-400 and N_4-CoS_2-500.

2.4. Preparation of nitrogen doped CoS_2 with different nitrogen amount

The nitrogen doping was regulated by a hydrogen reduction process of precursor. Briefly, the $Co(CO_3)_{0.5}(OH)$ $0.11H_2O$ was annealed under hydrogen atmosphere at 400 ºC with a heating rate of 10 °C/min and kept for 20 min. After cooling down to room temperature, the sample and 500 mg sulfur powder (at the upstream side) were placed separately in a quartz tube and the quartz tube was heated to 400 ºC under a heating rate of 10 °C/min and held for 40 min in nitrogen condition. The obtained sample was named as N_3-CoS_2-400. When the reduction reaction times were 40, 60 and 120 min, the final samples were donated as N_2-CoS_2-400, N_1-CoS_2-400 and N_0-CoS_2-400, respectively.

2.5. Characterization

Power X-ray diffraction (XRD) patterns were collected on a D8 ADVANCE diffractometer (Bruker, Germany) with Cu-Kα (1.5406 Å) radiation. Detailed chemical composition of samples was carried out by X-ray photoelectron spectroscopy (XPS, ESCALAB MKII, VG Co., United Kingdom) with Al-Kα X-ray radiation as the X-ray excitation source.

Morphological and lattice structural information were examined with Scanning Electron Microscope (SEM, Hitachi S-4800) and Transmission Electron Microscope (TEM, TECNAI G2). High-resolution TEM (HRTEM) images were obtained with an accelerating voltage of 200 kV.

2.6. Electrochemical Measurements

The electrochemical properties of all samples were investigated by a CHI 614D electrochemical workstation. In a three-electrode system, the prepared N doped CoS_2 was directly used as working electrode, while a Pt electrode and a mercury/mercury oxide electrode (MOE) served as counter electrode and reference electrode, respectively. To synthesis of the RuO_2 on CP, 1 mg of the RuO_2 and 4 wt% polytetrafluoroethylene were dispersed in 1 mL ethanol with sonication for 30 minutes to achieve a mixed solution, .then, 250 μL of this RuO_2 ink was drop-casted onto a 1 cm × 1 cm CP (loading 0.25 mg cm^{-2}) and dried naturally. The measured potentials vs. MOE were corrected to a reversible hydrogen electrode (RHE). Before electrochemical measurements, 1.0 M KOH solution was desecrated with argon for 30 min. EIS spectra were obtained in a frequency range from 10^{-2} to 10^6 Hz at 1.65 V vs. RHE [26].

3. RESULTS AND DISCUSSION

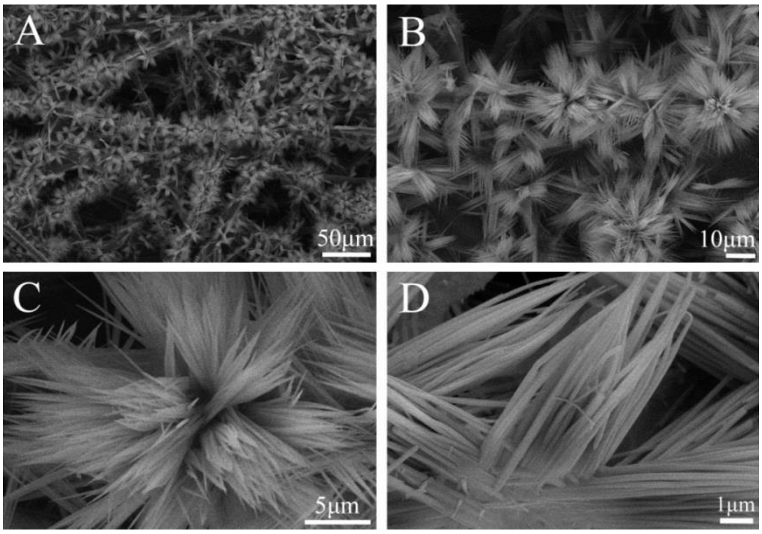

Figure 1. SEM images of $Co(CO_3)_{0.5}(OH)\ 0.11H_2O$ with different magnification. The scale bar of (A)-(D) are 50μm, 10μm, 5μm and 1μm, respectively.

We first synthesized flower-like nanoarray precursors functionalized with nitrogen-containing groups by a facile hydrothermal reaction. As shown in Figure 1A, the synthesized precursor is grown with high uniformity at a large scale on the CP. The precursor has a three dimensional flower-like morphology with an average size of 25 μm (Figure 1B). High resolution SEM images show that the flower-like nanoarrays consist of nanowires (Figure 1C). The average sizes of the nanowires are approximately 180 nm in diameter and 6 μm in length (Figure 1D). There are also some interval channels formed between neighboring units. The composition information of the synthesized precursor was analyzed by XRD (**Figure 2**). All diffraction peaks match well with the characteristics of a pure $Co(CO_3)_{0.5}(OH)\ 0.11H_2O$ phase with an orthorhombic structure (JCPDS No. 48-0083). The XPS spectrum verifies the presence of cobalt, oxygen, nitrogen, and carbon elements (Figure 3). By using a Gaussian fitting method, the Co 2p spectrum exhibits two prominent peaks at 782.4 and 798.4 eV, corresponding to the Co $2p_{3/2}$ and Co $2p_{1/2}$ spin–orbit peaks, respectively (Figure 3A).

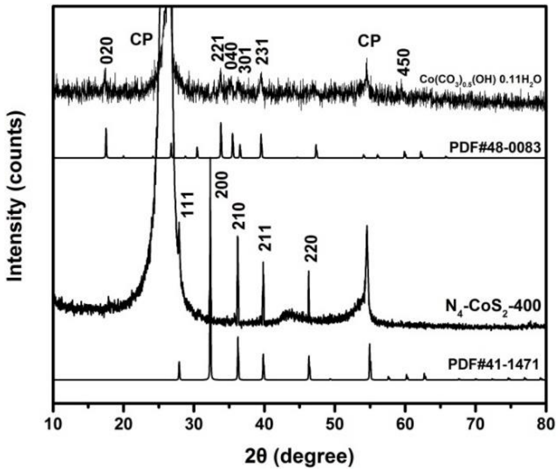

Figure 2. XRD patterns of $Co(CO_3)_{0.5}(OH)\ 0.11H_2O$ and N_4-CoS_2-400.

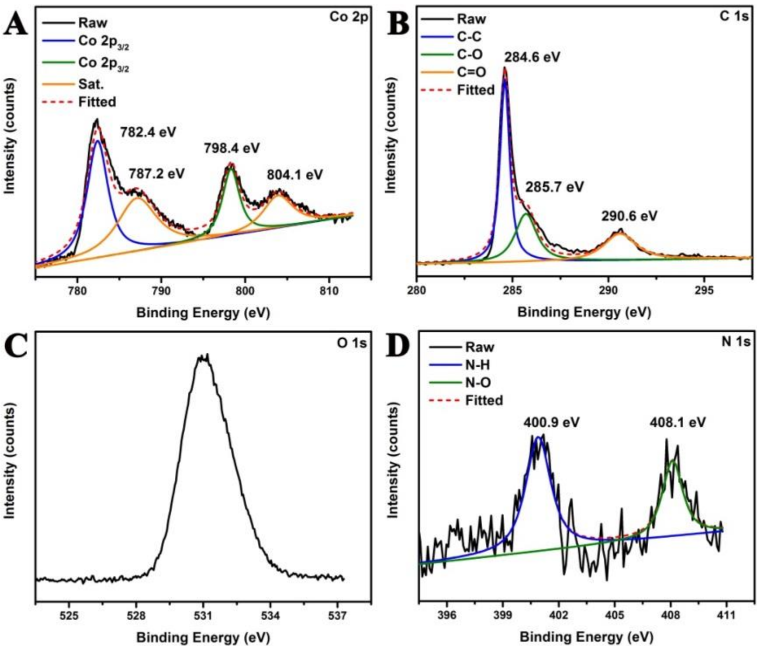

Figure 3. XPS spectrum of $Co(CO_3)_{0.5}(OH)\ 0.11H_2O$. (A) Co 2p, (B) C 1s, (C) O 1s and (D) N 1s.

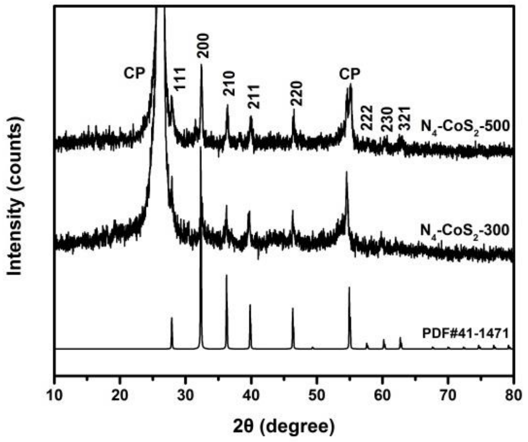

Figure 4. XRD patterns of N_4-CoS_2-300 and N_4-CoS_2-500.

The peaks at 787.2 and 804.1 eV correspond to satellite peaks. In the C 1s region (Figure 3B), three peaks are observed at 284.6, 285.7 and 290.6 eV, corresponding to C-C, C-O and C=O, respectively [27]. Two distinct peaks are clearly displayed in the high-resolution N 1s core level spectrum (Figure 3D), corresponding to N-H and N-O. [20] The above analysis indicates the successful synthesis of $Co(CO_3)_{0.5}(OH)$ $0.11H_2O$.

To obtain nitrogen doped CoS_2, a post annealing process was carried out in the presence of sulfur at 300°C, 400°C, 500°C for 40 min. The resultant samples are denoted as N_4-CoS_2-XXX hereafter, where XXX is the annealing temperature. After a series of sulfidation treatments, the characteristic peaks of $Co(CO_3)_{0.5}(OH)$ $0.11H_2O$ disappear completely. The resultant CoS_2 are well-crystallized in a cubic structure (JCPDS No. 41-1471), as confirmed by its XRD patterns in Figure 2 and Figure 4. The peak positions at $2\theta = 27.9^o$, 32.3^o, 36.2^o, 39.8^o and 46.3^o correspond to the (111), (200), (210), (211) and (220) planes. A top-view SEM image at low magnification of N_4-CoS_2-400 is shown in Figure 5A. The compactly arranged flower-like nanoarrays with average diameters of 25 μm are distributed uniformly on the CP. In high a magnification SEM image (Figure 5B), the flower-like nanoarrays also consist of nanowires, whereas the morphology becomes rougher compared with that of the precursor. This difference may cause by the relatively high annealing temperature, as the N_4-CoS_2-300 sample shows no morphological change after the sulfidation process (Figure 6A and B). When the temperature reaches 500^{o}C, the solid nanoparticles in the nanowire core can be clearly observed (Figure 5C and D). HRTEM was further used to examine the crystallographic nature of the N_4-CoS_2-400 sample. Figure 5C is a section of a CoS_2 nanowire with a highly ordered lattice fringe. The lattice fringes with an average spacing of 0.277 nm can be indexed to the (200) plane (Figure 5D).

The electrochemical activities of the various N_4-CoS_2-XXX catalysts toward OER are investigated in 1.0 M KOH in a three-electrode conformation. All potentials used are referenced to a RHE (see the Experimental section for details). As shown in Figure 7A, the N_4-CoS_2-400 shows the highest current response with an overpotential of 290 mV to provide the current density of 10 mA cm^{-2} (Figure 7B), which is comparable to the values reported thus far for most active transition metal dichalcogenides (Table 1).

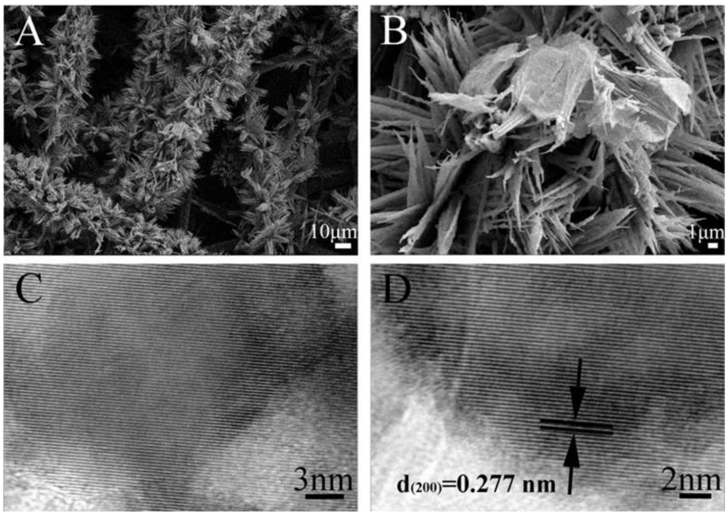

Figure 5. SEM images (A, B) and HRTEM image (C, D) of N_4-CoS_2-400.

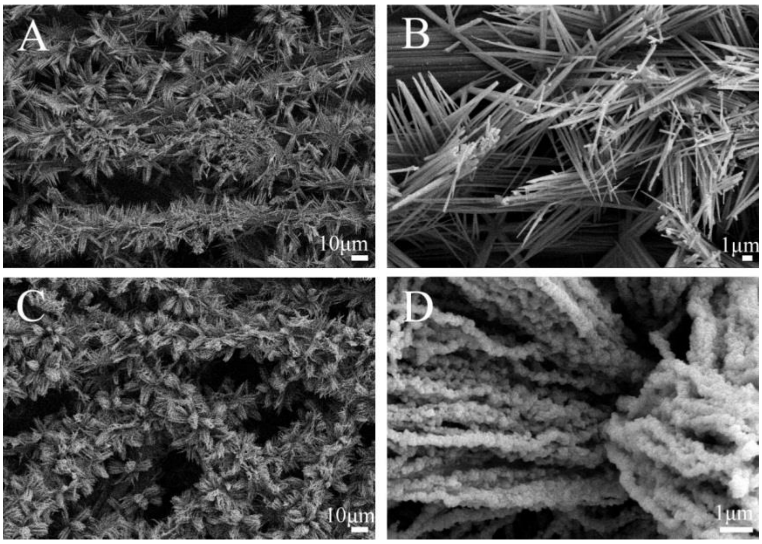

Figure 6. SEM images of N_4-CoS_2-300 (A, B) and N_4-CoS_2-500 (C, D).

Moreover, an extremely large current density, which is positively related to the amount of oxygen evolution on the surface, is 300 mA cm^{-2} with overpotential of 520 mV. The electrode kinetics for OER was further measured by electrochemical impedance spectroscopy (EIS), as shown in Figure 7D and Table 2. The N_4-CoS_2-500 sample has the smallest charge transfer resistance (R_2), while the N_4-CoS_2-300 sample exhibits the largest charge transfer resistance. An increase in the sulfidation temperature significantly enhances the charge transfer process. Additionally, Table 2 also shows that the difference in R_2 values between the N_4-CoS_2-500 and N_4-CoS_2-400 samples is quite small. The electrochemical surface area (ECSA) was further evaluated by an electrical double-layer capacitor (C_{dl}) at the interface. The C_{dl} is proportional to the slope of the current density differences against the scan rate curves, which is obtained by measuring the CV curves in a non-Faradaic region (Figure 8). As shown in Figure 7C, the N_2-CoS_2-400 sample shows the highest slope values. However, the insignificant difference in C_{dl} values suggests that the excellent OER performance of the N_4-CoS_2-400 has no correlation with its larger ECSA in comparison with that of the N_4-CoS_2-300 and N_4-CoS_2-500 samples. Overall, the N_4-CoS_2-400 sample shows the best electrochemical activity toward OER.

Table 1. Transitional metal dichalcogenides-based OER electrocatalysts and their performance.

Electrocatalyst	Overpotential (mV)/ mA cm^{-2}	Electrolyte solution	Ref.
N_4-CoS_2-400	290/η_{10}	1 M KOH	This work
CeO_x/CoS	269/η_{10}	1M KOH	[28]
MoS_2/Ni_3S_2	218/η_{10}	1M KOH	[29]
NiS_2/Ti foam	330/η_{10}	1M KOH	[30]
High index Ni_3S_2	260/η_{10}	1M KOH	[31]

Pt-CoS_2/CC	300/η_{10}	1M KOH	[32]
N-$NiMoO_4$/NiS_2	267/η_{10}	1M KOH	[33]
NiS Film	320/η_{10}	1M KOH	[34]
NiS/ Ni foam	335/η_{50}	1M KOH	[35]
Porous hollow NiS	320/η_{10}	1M KOH	[36]
NiS@Stainless steel mesh	297/η_{10}	0.1M KOH	[37]
FeS_2/CoS_2	302/η_{100}	1M KOH	[38]
NiS/ Ni foam	340/η_{30}	1M KOH	[39]
NiS Nanowire array	300/η_{10}	1M KOH	[40]

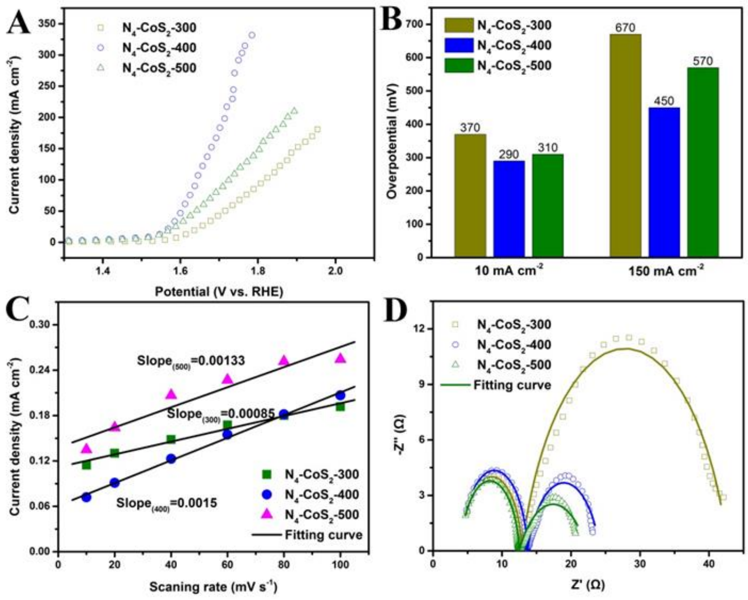

Figure 7. (A) Polarization curves of N_4-CoS_2-300, N_4-CoS_2-400 and N_4-CoS_2-500 in 1.0 M KOH at a scan rate of 2 mV s^{-1}. (B) Overpotentials to afford different current density. (C) Current density differences (Δj) plotted against scan rates. (D) Nyquist plots of EIS spectra measured from N_4-CoS_2-300, N_4-CoS_2-400 and N_4-CoS_2-500 at the overpotential of 350 mV.

Table 2. The fitting results of EIS spectra shown in Figure 7D using the equivalent circuit in their inset.

Sample	R_s (Ω)	CPE_1 (F·cm^{-2})	n_1	R_1 (Ω)	CPE_2 (F·cm^{-2})	n_2	R_2 (Ω)
N_4-CoS_2-300	4.17	$1.61e^{-7}$	0.95	8.71	0.025	0.81	29.88
N_4-CoS_2-400	4.07	$1.69e^{-7}$	0.94	9.62	0.11	0.78	10.52
N_4-CoS_2-500	3.98	$2.31e^{-7}$	0.93	8.5	0.11	0.6	9.84

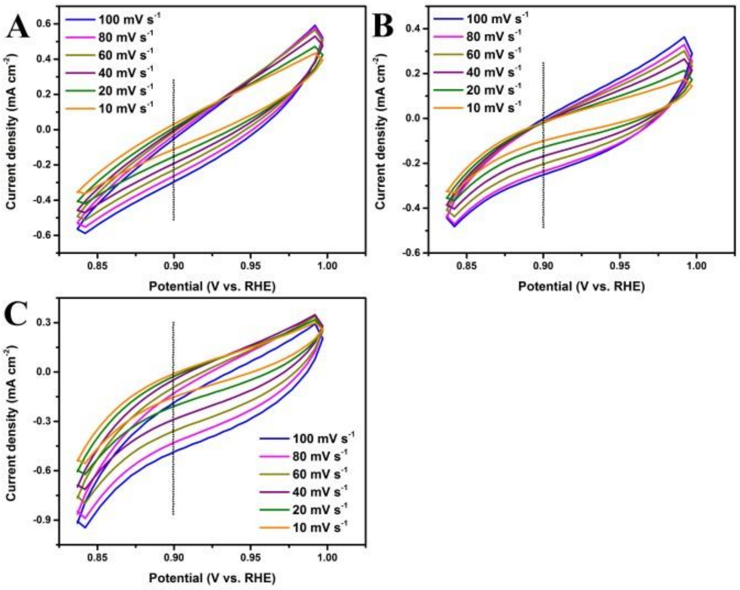

Figure 8. CV curves of N$_4$-CoS$_2$-300 (A), N$_4$-CoS$_2$-400 (B) and N$_4$-CoS$_2$-500 (C) at different scan rates.

Controlling and modulating the electronic structure is considered an efficient means of adjusting the energy band structure for intermediate adsorption. Energy-level engineering is generally employed via heteroatom doping, which facilitates the *d* band center to the Fermi level [41]and, reduces the reaction barrier toward the OER. XPS results indicate the presence of nitrogen in the N$_4$-CoS$_2$-400 sample (Figure 12). As a kind of heteroatom, nitrogen has a significant effect on the position of the adjacent metal *d* band center, electron density, and Gibbs free energy of different intermediate adsorption [20, 21, 42]. The nitrogen atoms adjacent to the metal atoms possess well-defined electronic configurations and ideal active sites for intermediate adsorption, thus reducing the reaction barriers of OER. In this scenario, we further examined the influence of the amount nitrogen doping on the electrochemical activity toward OER.

Samples containing less nitrogen were first treated by annealing the precursor with hydrogen (5%) for different times. The resultant samples are denoted as N$_4$-CoS$_2$-400-H$_{ZZZ}$ hereafter, where ZZZ is used to distinguish the different reaction times (see the Experimental section for details). After the post sulfidation process, different nitrogen containing samples are obtained. The resultant samples are denoted as N$_{YYY}$-CoS$_2$-400 hereafter, where YYY is used to distinguish the different amount of nitrogen doping (see the Experimental section for details). The N percentage was confirmed by an elemental analyzer (EA) analysis. After these treatments, the amount of nitrogen doping significantly decreased (Table 3). The electrochemical activities toward the OER of the different samples were then examined by linear sweep voltammetry measurements. The data shows a clear monotonic trend, in which decreasing nitrogen content results in increased overpotentials to obtain a specified current density (Figure 9A). This implies the importance of nitrogen doping. Notably, the smallest nitrogen containing sample N$_1$-CoS$_2$-400 needs a small overpotential of 330 mV to drive a current density of 10 mA cm^{-2}, while 370 mV is needed for N$_0$-CoS$_2$-400, which is sample without nitrogen(Figure 9B). It should be noted that the relatively inactive sample N_4-CoS_2-300 also shows superior performance toward OER compared with that of N_0-CoS_2-400 (Figure 10).

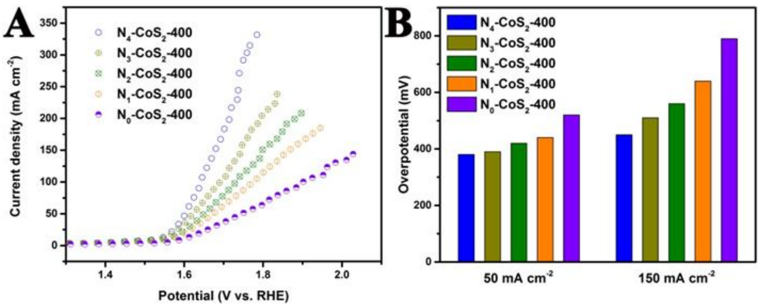

Figure 9. (A) Polarization curves of N_4-CoS_2-400, N_3-CoS_2-400, N_2-CoS_2-400, N_1-CoS_2-400 and N_0-CoS_2-400 in 1.0 M KOH at a scan rate of 2 mV s^{-1}. (B) Overpotentials to afford different current density.

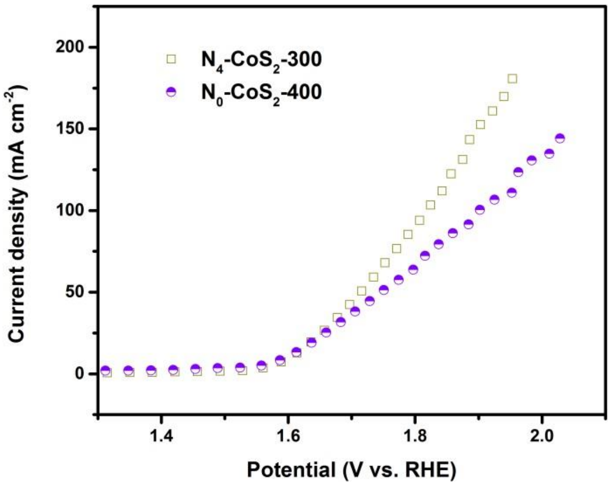

Figure 10. Polarization curves of N_4-CoS_2-300 and N_0-CoS_2-400 in 1.0 M KOH at a scan rate of 2 mV s^{-1}.

Table 3 Nitrogen doping properties between different products.

Sample	N_4-CoS_2-400	N_3-CoS_2-400	N_2-CoS_2-400	N_1-CoS_2-400	N_0-CoS_2-400
Nitrogen doping (w%)	13.6%	8.1%	4.3%	2.8%	0

XRD measurements were employed to monitor the structural breathing of nitrogen-doped CoS_2 during hydrogen treatment. As shown in Figure 11, all the XRD patterns can be indexed to pure CoS_2 with a cubic structure (JCPDS No. 41-1471). Then, XPS was employed to analyze the chemical bonding states of each element on the surface, and fitting parameters are shown in Table 4. Figure 12A shows the Co 2p peak of nitrogen-doped CoS_2, which consists of six multiple peaks arising from the Co^{3+} oxidation states (779.1 and 794.3 eV), Co^{2+} oxidation states (781.5 and 798.7 eV), and satellite peaks (786.5 and 803.3 eV). In comparison, the core level spectrum of the Co 2p region of N_0-CoS_2-400 has four peaks without doublets. The core level spectrum of the S 2p region is divided into two spin-orbit doublets (Figure 12B). The first doublet is observed at approximately 161.7 and 162.6 eV, corresponding to the S $2p_{1/2}$ and S $2p_{3/2}$ orbitals of terminal sulfur (as shown in Figure 13). The second doublet is observed at approximately 162.9 and 164.1 eV, suggesting the existence of bridging sulfur or apical sulfur.[42] The data shows a clear monotonic trend, in which decreasing nitrogen content results in an increased terminal sulfur ratio. A decrease in terminal sulfur indicates an increase in terminal cobalt or terminal nitrogen. The former can provide more active sites and the latter can activate more adjacent cobalt, both resulting in an improvement of electrochemical activity toward OER.[20, 21] This may explain the electrochemical difference between various nitrogen containing samples. In addition, N 1s spectra verify the change of chemical bonding states along with a decrease in nitrogen. (Figure 12C).

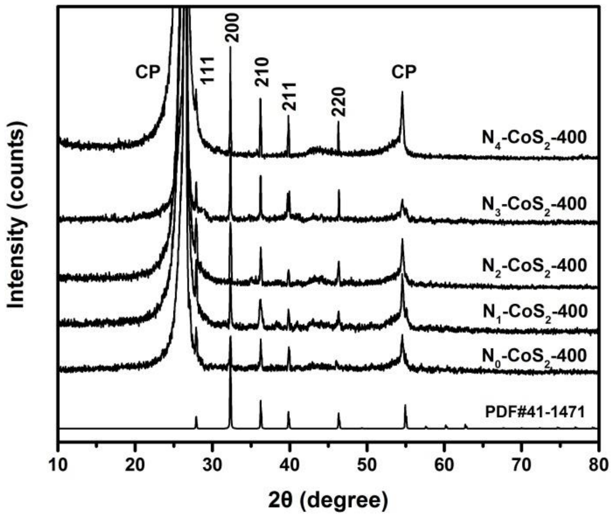

Figure 11. XRD patterns of N_4-CoS_2-400, N_3-CoS_2-400, N_2-CoS_2-400, N_1-CoS_2-400 and N_0-CoS_2-400.

Table 4. Fitting parameters used for the decomposition of Co 2p and S 2p XPS spectra

Components	N_4-CoS_2-400		N_3-CoS_2-400		N_2-CoS_2-400	
	Peak (eV)	FWHM (eV)	Peak (eV)	FWHM (eV)	Peak (eV)	FWHM (eV)
Co	779.3	1.69	778.9	1.74	779.1	0.92
	782.2	3.45	782.0	3	781.5	4.01
	786.8	4.32	786.8	4.02	786.5	5
	794.6	4	794.0	3.05	794.3	2.68
	798.5	3	798.7	3.48	798.7	3.2
	803.3	5.47	803.3	4.22	803.3	3.47
	N_1-CoS_2-400		N_0-CoS_2-400			

Components	Peak (eV)	FWHM (eV)	Peak (eV)	FWHM (eV)		
Co	778.8	0.91	781.2	4.1		
	782.9	3.71	786.5	3.3		
	787.3	5	797.0	3.5		
	793.7	2.66	802.9	3.4		
	799.1	2.78				
	803.8	5				
Components	N_4-CoS_2-400		N_3-CoS_2-400		N_2-CoS_2-400	
	Peak (eV)	FWHM (eV)	Peak (eV)	FWHM (eV)	Peak (eV)	FWHM (eV)
S	163.1	1	161.9	1	162.0	1
	164.2	1	162.8	1	162.9	1
			163.1	1	163.2	1
			164.2	1	164.2	1
Components	N_1-CoS_2-400		N_0-CoS_2-400			
	Peak (eV)	FWHM (eV)	Peak (eV)	FWHM (eV)		
S	161.8	1	161.7	1		
	162.8	1	162.6	1		
	163.1	1	162.9	1		
	164.2	1	164.1	1		

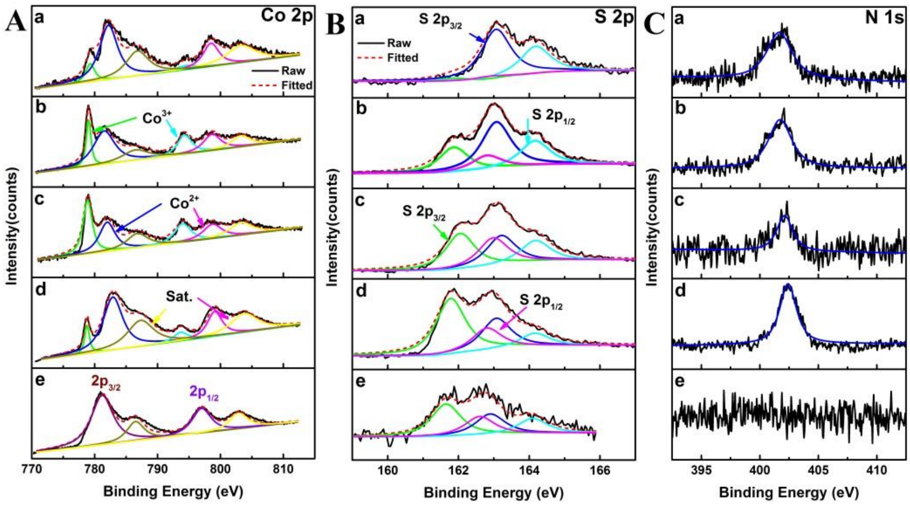

Figure 12. XPS spectra of N_4-CoS_2-400 (a), N_3-CoS_2-400 (b), N_2-CoS_2-400 (c), N_1-CoS_2-400 (d) and N_0-CoS_2-400 (e).

We further examined the morphology of different nitrogen doped samples. When treated with hydrogen (5%) at 400°C for 20 min, the obtained N_3-CoS_2-400 sample shows a similar morphology to N_4-CoS_2-400 (Figure 13). When the reaction time is extended to 40 min, the obtained nanowires become rougher, and some of them break down into small pieces (Figure 14). When the reaction time is 60 min, even the N_4-CoS_2-400-H_{60} becomes rougher than that of the precursor (Figure 15). After sulfidation, the nanowires in N_2-CoS_2-400 aggregate forming a sheet-like morphology, and solid nanoparticles in the sheet can be clearly observed (Figure 14). Further increasing the reaction time to 120 min shows that the aggregation becomes more serious, and some large nanoparticles begin to appear (Figure 16). The above morphology changes seem to also be responsible for the electrochemical difference. During OER, the morphology difference mainly affects the number of active sites. In light of the above results, we further examined the ECSA of different samples. As shown in Figure 17, N_2-CoS_2-400 shows the largest ECSA, while the N_3-CoS_2-400 shows the smallest value. Combining the SEM and ECSA results, the difference in number of active site is not a key factor for the electrochemical activity in this situation. The electrochemical performance is largely related to ion diffusion and charge transfer kinetics, and EIS provides compelling evidence to describe the properties of an OER electrode.

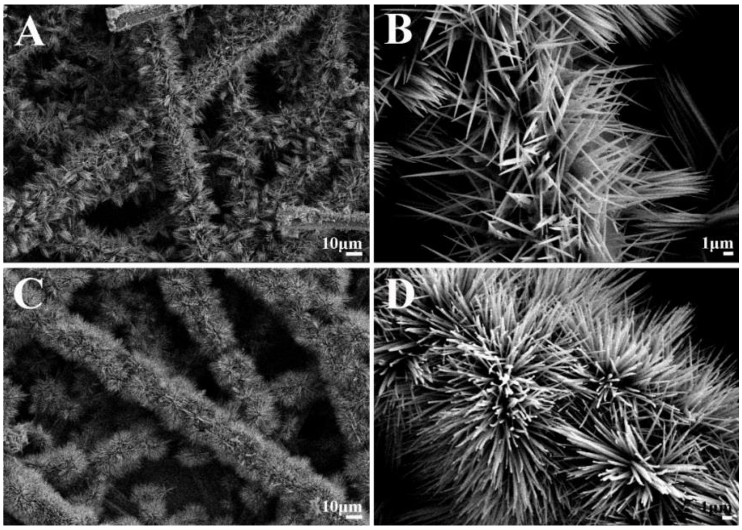

Figure 13. SEM images of N_4-CoS_2-400-H_{20} (A, B) and N_3-CoS_2-400 (C, D).

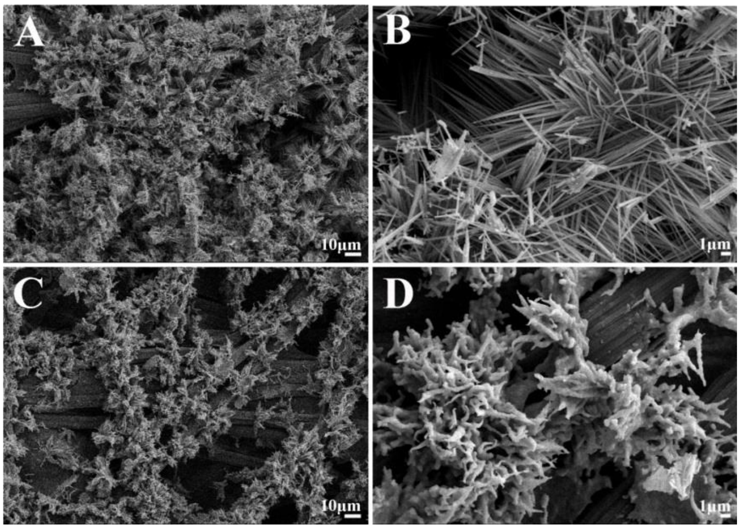

Figure 14. SEM images of N_4-CoS_2-400-H_{40} (A, B) and N_2-CoS_2-400 (C, D).

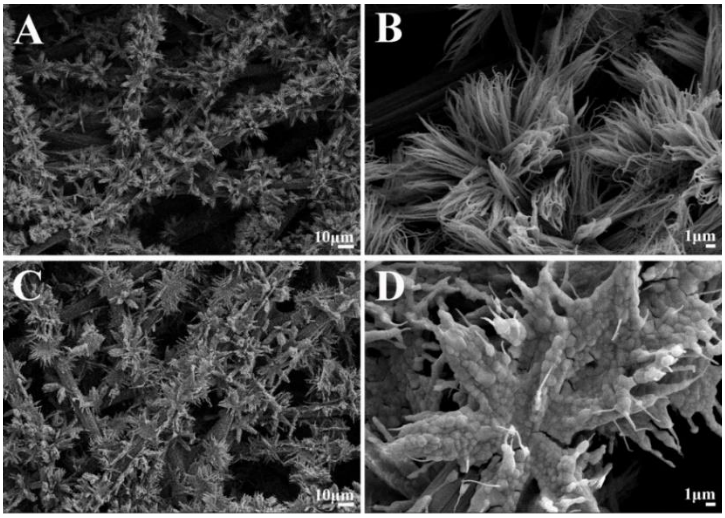

Figure 15. SEM images of N_4-CoS_2-400-H_{60} (A, B) and N_1-CoS_2-400 (C, D).

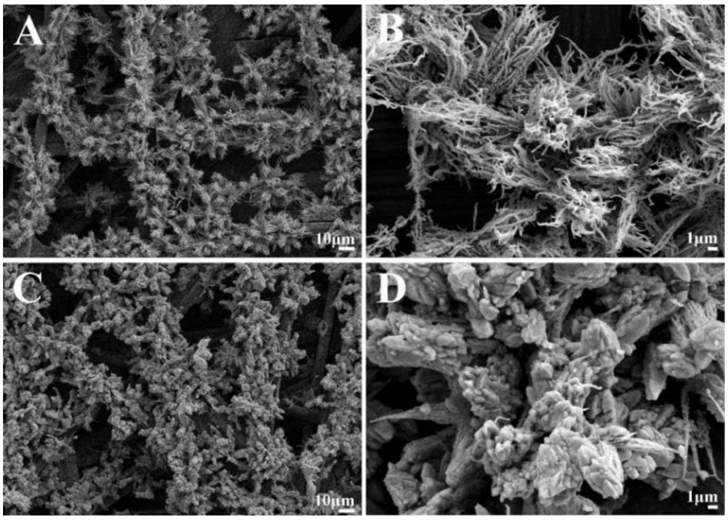

Figure 16. SEM images of N_4-CoS_2-400-H_{120} (A, B) and N_0-CoS_2-400 (C, D).

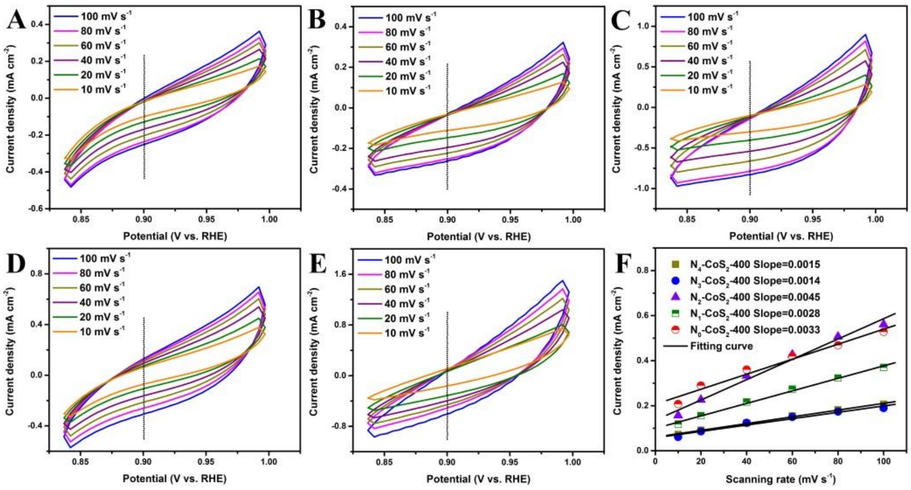

Figure 17. CV curves of N_4-CoS_2-400 (A), N_3-CoS_2-400 (B), N_2-CoS_2-400 (C), N_1-CoS_2-400 (D) and N_0-CoS_2-400 (E) at different scan rates. Current density differences (Δj) plotted against scan rates (D).

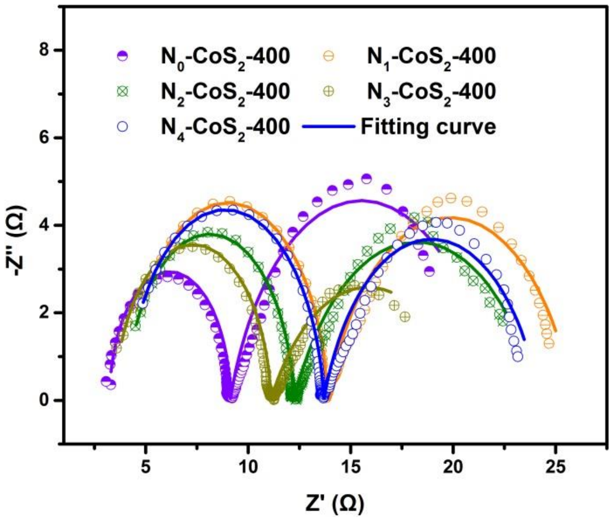

Figure 18. Nyquist plots of EIS spectra measured from N_4-CoS_2-400, N_3-CoS_2-400, N_2-CoS_2-400, N_1-CoS_2-400 and N_0-CoS_2-400 at the overpotential of 350 mV.

Table 5. The fitting results of EIS spectra shown in Figure 15 using the equivalent circuit in their inset.

Sample	R_s (Ω)	CPE_1 ($F \cdot cm^{-2}$)	n_1	R_1 (Ω)	CPE_2 ($F \cdot cm^{-2}$)	n_2	R_2 (Ω)
N_0-CoS_2-400	3.24	$2.45e^{-7}$	0.99	5.90	0.093	0.82	11.8
N_1-CoS_2-400	4.15	$1.41e^{-7}$	0.95	9.72	0.098	0.77	12
N_2-CoS_2-400	4	$1.85e^{-7}$	0.95	8.23	0.12	0.69	11.95
N_3-CoS_2-400	3.49	$2.57e^{-7}$	0.96	7.61	0.16	0.64	9.48
N_4-CoS_2-400	4.07	$1.69e^{-7}$	0.94	9.62	0.11	0.78	10.52

As shown in Figure 18 and Table 5, the N_3-CoS_2-400 sample shows the smallest R_2 value, indicating its fast charge transfer kinetics. However, the difference in the R_2 value between different nitrogen containing samples is quite small, implying that the charge transfer process is minor influence on the OER performance.

4. CONCLUSIONS

In summary, nitrogen-doped CoS_2 was fabricated through an annealing process by using nitrogen containing $Co(CO_3)_{0.5}(OH)_{0.5}$ $0.11H_2O$ as a precursor. Notably, a N_4-CoS_2-400 sample exhibits a small overpotential of 290 mV to afford a current density of 10 mA cm^{-2}. We further explored the influence of nitrogen doping by varying the heteroatom amount through a hydrogen reduction process. Nitrogen doping can affect the terminal sulfur ratio. A decrease in the terminal sulfur ratio leads to more cobalt or nitrogen exposure on the surface. The exposure of cobalt means a more active site, which is considered beneficial for improving the reaction rate. The exposure of nitrogen can activate adjacent cobalt atom, which reducing the high reaction barriers for intermediate adsorption. Both of these situations can greatly promote electrochemical processes toward OER. These excellent properties provided by nitrogen doping make it a powerful tool for a wide range of potential applications in energy-related fields.

ACKNOWLEDGEMENTS

This work was financially supported by the National Natural Science Foundation of China (21878134), the Natural Science Foundation of Jiangsu Province (BK20161363) and the Jiangsu Postdoctoral Foundation (1601091B).

References

1. Z.W. Seh, J. Kibsgaard, C.F. Dickens, I. Chorkendorff, J.K. Nørskov and T.F. Jaramillo, *Science*, 355 (2017) 6321.
2. L. Han, S. Dong and E. Wang, *Adv. Mater.*, 28 (2016) 9266.
3. N. T. Suen, S. F. Hung, Q. Quan, N. Zhang, Y. J. Xu and H.M. Chen, *Chem. Soc. Rev.*, 46 (2017) 337; X. Xu, W. Zhong, L. Zhang, G. Liu and Y. Du, *J. Colloid Interface Sci.*, 24 (2019) 556.
4. Y. Yan, B.Y. Xia, Z.C. Xu and X. Wang, *ACS Catal.*, 4 (2014) 1693.
5. B. Hinnemann, P.G. Moses, J. Bonde, K.P. Jørgensen, J.H. Nielsen, S. Horch, I. Chorkendorff and J.K. Nørskov, *J. Am. Chem. Soc.*, 127 (2005) 5308.
6. Z. Lei, J. Zhan, L. Tang, Y. Zhang and Y. Wang, *Adv. Energy Mater.*, 8 (2018) 1703482.
7. T. Sun, J. Wang, X. Chi, Y.X. Lin, Z.X. Chen, X. Ling, C.T. Qiu, Y.S. Xu, L. Song, W. Chen and C.L. Su, *ACS Catal.*, 8 (2018) 7585.
8. J. Tao, S. Chen, L. Guan, G. Chen, C. Yu, L. Chen, X. Cheng, H. Zhang and X. Xie, *Electrochim. Acta,* 283 (2018) 419.
9. L. L. Feng, G. Yu, Y. Wu, G. D. Li, H. Li, Y. Sun, T. Asefa, W. Chen and X. Zou, *J. Am. Chem. Soc.*, 137 (2015) 14023.
10. M.S. Faber, R. Dziedzic, M.A. Lukowski, N.S. Kaiser, Q. Ding and S. Jin, *J. Am. Chem. Soc.*, 28 (2014) 10053.
11. D. Kong, J.J. Cha, H. Wang, H.R. Lee and Y. Cui, *Energy Environ. Sci.,* 6 (2013) 3553.
12. J. Tian, Q. Liu, A.M. Asiri and X. Sun, *J. Am. Chem. Soc.*, 136 (2014) 7587.
13. J. Kibsgaard, C. Tsai, K. Chan, J.D. Benck, J.K. Norskov, F. Abild-Pedersen and T.F. Jaramillo, *Energy Environ. Sci.,* 8 (2015) 3022.
14. B. Han, K.A. Stoerzinger, V. Tileli, A.D. Gamalski, E.A. Stach and Y. Shao-Horn, *Nat. Mater.,* 16 (2017) 121.
15. Y. Liu, H. Cheng, M. Lyu, S. Fan, Q. Liu, W. Zhang, Y. Zhi, C. Wang, C. Xiao, S. Wei, B. Ye and Y. Xie, *J. Am. Chem. Soc.*, 136 (2014) 15670.
16. M. Retuerto, L. Pascual, F. Calle-Vallejo, P. Ferrer, D. Gianolio, A.G. Pereira, Á. García, J. Torrero, M.T. Fernández-Díaz, P. Bencok, M.A. Peña, J.L.G. Fierro and S. Rojas, *Nat. Commun.,* 10 (2019) 2041.
17. T. Ouyang, Y. Q. Ye, C. Y. Wu, K. Xiao and Z. Q. Liu, *Angew. Chem., Int. Ed.,* 58 (2019) 4923.
18. M. Caban-Acevedo, M.L. Stone, J.R. Schmidt, J.G. Thomas, Q. Ding, H. C. Chang, M. L. Tsai, J. H. He and S. Jin, *Nat. Mater.,* 14 (2015) 1245.
19. B. Zhang, X. Zheng, O. Voznyy, R. Comin, M. Bajdich, M. García-Melchor, L. Han, J. Xu, M. Liu, L. Zheng, F.P. García de Arquer, C.T. Dinh, F. Fan, M. Yuan, E. Yassitepe, N. Chen, T. Regier, P. Liu, Y. Li, P. De Luna, A. Janmohamed, H.L. Xin, H. Yang, A. Vojvodic and E.H. Sargent, *Science,*

352 (2016) 333.
20. J. Hao, W. Yang, Z. Peng, C. Zhang, Z. Huang and W. Shi, *ACS Catal*., 7 (2017) 4214.
21. J. Hao, W. Yang, J. Hou, B. Mao, Z. Huang and W. Shi, *J. Mater. Chem. A,* 5 (2017) 17811.
22. Y. Li, F. Li, Y. Zhao, S. Li and Y. Chen, *J. Mater. Chem. A,* 7 (2019) 20658.
23. A. Gupta, W.D. Chemelewski, C. Buddie Mullins and J.B. Goodenough, *Adv. Mater*., 27 (2015) 6063.
24. Y. Zhu, X. Liu, S. Jin, H. Chen and Y. Chen, *J. Mater. Chem. A*, 7 (2019) 5875.
25. J. Hao, W. Yang, Z. Huang and C. Zhang, *Adv. Mater. Interfaces* ,3 (2016) 1600236.
26. S. Shi, M. Zhang, Y. Liu and G. Yang, *J. Alloy. Compd*., 764 (2018) 709.
27. H. Xu, J. Cao, C. Shan, B. Wang, P. Xi, W. Liu and Y. Tang, *Angew. Chem., Int. Ed.*, 57 (2018) 8654.
28. B. Zhang, X. Zheng, O. Voznyy, R. Comin, M. Bajdich, M. García-Melchor, L. Han, J. Xu, M. Liu, L. Zheng, F. P. García de Arquer, C. T. Dinh, F. Fan, M. Yuan, E. Yassitepe, N. Chen, T. Regier, P. Liu, Y. Li, P. De Luna, A. Janmohamed, H. L. Xin, H. Yang, A. Vojvodic and E. H. Sargent, *Science*, 352 (2016) 333.
29. L. Yang, M. Gao, B. Dai, X. Guo, Z. Liu and B. Peng, *Electrochim. Acta*, 191 (2016) 813.
30. L. L. Feng, G. Yu, Y. Wu, G. D. Li, H. Li, Y. Sun, T. Asefa, W. Chen and X. Zou, *J. Am. Chem. Soc.*, 137 (2015) 14023.
31. X. Han, X. Wu, Y. Deng, J. Liu, J. Lu, C. Zhong and W. Hu, *Adv. Energy Mater.*, 8 (2018) 1800935.
32. L. An, J. Feng, Y. Zhang, R. Wang, H. Liu, G.C. Wang, F. Cheng and P. Xi, *Adv. Funct. Mater.*, 28 (2018) 1805298.
33. O. Mabayoje, A. Shoola, B. R. Wygant and C. B. Mullins, *ACS Energy Lett.,* 1 (2016) 195.
34. W. Zhu, X. Yue, W. Zhang, S. Yu, Y. Zhang, J. Wang and J. Wang, *Chem. Commun*., 52 (2016) 1486.
35. P. Luo, H. Zhang, L. Liu, Y. Zhang, J. Deng, C. Xu, N. Hu and Y. Wang, *ACS Appl. Mater. Interfaces*, 9 (2017) 2500.
36. J. S. Chen, J. Ren, M. Shalom, T. Fellinger and M. Antonietti, *ACS Appl. Mater. Interfaces*, 8 (2016) 5509.
37. Y. Li, J. Yin, L. An, M. Lu, K. Sun, Y. Q. Zhao, D. Gao, F. Cheng and P. Xi, *Small*, 14 (2018) 1801070.
38. G. F. Chen, T. Y. Ma, Z. Q. Liu, N. Li, Y. Z. Su, K. Davey and S. Z. Qiao, *Adv. Funct. Mater.*, 26 (2016) 3314.
39. A. Sivanantham, P. Ganesan and S. Shanmugam, *Adv. Funct. Mater.*, 26 (2016) 4661.
40. J. Hao and W. Shi, *Chin. J. Catal*., 39 (2018) 1157.
41. P. Chen, T. Zhou, M. Chen, Y. Tong, N. Zhang, X. Peng, W. Chu, X. Wu, C. Wu and Y. Xie, *ACS Catal.,* 7 (2017) 7405.
42. J. Kibsgaard, T.F. Jaramillo and F. Besenbacher, *Nat. Chem*., 6 (2014) 248.